ELSEVIER

International Journal of Solids and Structures 41 (2004) 5541–5563

INTERNATIONAL JOURNAL OF SOLIDS and STRUCTURES

www.elsevier.com/locate/ijsolstr

Plane strain bifurcation analysis of soils by the tangential–subloading surface model

Mehdi Khojastehpour [a,*], Koichi Hashiguchi [b,*]

[a] *Department of Mechanical Engineering Science, Graduate School of Engineering, Kyushu University, Hakozaki 6-10-1, Higashi-ku, Fukuoka 812-8581, Japan*

[b] *Graduate School, Division of Bioproduction Environmental Science, Kyushu University, Hakozaki 6-10-1, Higashi-ku, Fukuoka 812-8581, Japan*

Received 6 April 2004; received in revised form 6 April 2004
Available online 5 June 2004

Abstract

The tangential–subloading surface model can describe the normal-plastic strain rate due to the rate of stress inside the yield surface and the tangential-plastic strain rate due to the stress rate component tangential to the subloading surface. The localized and diffuse bifurcation modes of the rectangular soil specimen subjected to plane strain loading under the undrained conditions are analyzed by adopting the tangential–subloading surface model, exhibiting the characteristic regimes of the governing equations (elliptic, hyperbolic and parabolic) in this article. Further, the conditions for shear band formation, shear band inclination, diffuse bifurcation modes, and the long and short wavelength limit of diffuse modes are discussed in relation to material properties and the state of stress, i.e. the stress-ratio and the normal-yield ratio. The tangential-plastic strain rate makes the inception of bifurcation modes easier in not only normal-yield, but also subyield states.

Keywords: Bifurcation; Shear band; Elastoplasticity; Soil; Subloading surface model

1. Introduction

Plastic instability phenomenon is an important problem in geomechanics in relation to the progressive failure of geostructures. It is induced by material softening and geometrical nonlinearity and leads to the *bifurcation of deformation* such as diffuse geometric modes (bulging and buckling) and localized modes (shear band).

Localized and *diffuse* bifurcation modes of deformation, so-called *shear band* and, *bulging* or *buckling*, respectively, in materials are widely observed when a deformation becomes large, approaching a failure. The occurrence of localized and diffuse bifurcation modes is unavoidable even in the element test of a

* Corresponding authors. Tel.: +81-92-642-3381; fax: +81-92-641-9744 (M. Khojastehpour), fax: +81-92-642-2932 (K. Hashiguchi).
E-mail addresses: mkhpour@mech.kyushu-u.ac.jp (M. Khojastehpour), khashi@bpes.kyushu-u.ac.jp (K. Hashiguchi).

0020-7683/$ - see front matter © 2004 Elsevier Ltd. All rights reserved.
doi:10.1016/j.ijsolstr.2004.04.017

material specimen, even though every effort is made to prevent inhomogeneity of deformation. The formation of localized and diffuse bifurcation modes can be regarded as *bifurcation* from a homogeneous fundamental path that can hold only in an unstable manner, resulting in so-called *material instability*.

Various theoretical interpretations for the localized and diffuse bifurcation modes of deformation (Hill and Hutchinson, 1975; Rudnicki and Rice, 1975; Young, 1976; Needleman, 1979; Vardoulakis, 1980, 1981; Yatomi et al., 1989; Chau and Rudnicki, 1990; Bardet, 1991; Iizuka et al., 1992; Papamichos and Vardoulakis, 1995, etc.) have been attempted up to the present. Their results suggest a deficiency in the traditional elastoplastic constitutive equations (cf. Schofield and Wroth, 1968; Bousshine et al., 2001; Peric and Ayari, 2002) in which the plastic strain rate is independent of the stress rate component tangential to the yield/loading surface, letting stress rate component tangential to the yield/loading surface and its influence on the inelastic strain rate be called the *tangential stress rate* and the *tangential stress rate effect*. The tangential stress rate effect has been experimentally measured by Ishihara and Towhata (1983), Miura et al. (1986), Pradel et al. (1990) and Gutierrez et al. (1991) for soils.

As reviewed by Hashiguchi (1997) and Hashiguchi and Tsutsumi (2001), various elastoplastic constitutive equations extended to describe the tangential stress rate effect have been proposed. Among them, however, the model proposed by Hashiguchi and Tsutsumi (2001) is applicable to an arbitrary loading process, including an unloading and a reloading process, fulfilling the mechanical requirements for constitutive equations (Hashiguchi, 1993a,b, 1997), i.e. the continuity condition, the smoothness condition, the Masing effect and the work rate-stiffness relaxation. It is formulated by introducing an additional strain rate, named *tangential-plastic strain rate*, induced by the *deviatoric tangential stress rate* into the subloading surface model (Hashiguchi and Ueno, 1977; Hashiguchi, 1980, 1989; Hashiguchi et al., 2002). It is of a simple form of rate-linearity enabling a reciprocal expression, i.e. the analytical expression of strain rate in terms of stress rate and its inverse expression, and keeps the symmetry of the stiffness modulus, thus leading to convenient analyses of boundary value problems.

The present article extends the pervious bifurcation analyses of a rectangular specimen subjected to plane strain loading by Hill and Hutchinson (1975), Young (1976), Needleman (1979), Vardoulakis (1981), Chau and Rudnicki (1990), Hashiguchi and Khojastehpour (2003) to include subloading surface model with tangential stress rate effect (Hashiguchi and Tsutsumi, 2001; Hashiguchi, in press) for soils. In this article, the constitutive equation of soils will be first reviewed briefly, in which the material functions of soils are incorporated into the subloading surface model with the tangential stress rate effect. This is applicable to soils in not only normal-yield, but also subyield states, for not only lower but also higher stress ratio than the critical state. Then, based on the constitutive equation, the localized and diffuse bifurcation modes of a rectangular soil specimen subjected to plane strain loading under the undrained conditions are analyzed and the characteristic regimes, elliptic, hyperbolic or parabolic, are identified depending on the state of stress and material parameters. Further, the conditions for shear band formation, shear band inclination, diffuse bifurcation modes, and the long and short wavelength limit of diffuse modes are discussed in relation to the material properties and the state of stress.

2. Outline of the tangential–subloading surface model

Denoting the current configuration of the material particle as $\mathbf{x}$ and the current velocity as $\mathbf{v}$, the velocity gradient is described as $\mathbf{L} = \partial\mathbf{v}/\partial\mathbf{x}$, by which the strain rate and the continuum spin are defined as $\mathbf{D}$ $(= (\mathbf{L} + \mathbf{L}^{\mathrm{T}})/2)$ and $\mathbf{W}$ $(= (\mathbf{L} - \mathbf{L}^{\mathrm{T}})/2)$, respectively, $(\ )^{\mathrm{T}}$ standing for the transpose.

Now let it be assumed that the strain rate $\mathbf{D}$ is additively decomposed into the elastic strain rate $\mathbf{D}^{\mathrm{e}}$ and the inelastic strain rate $\mathbf{D}^{\mathrm{i}}$, i.e.

$$\mathbf{D} = \mathbf{D}^{\mathrm{e}} + \mathbf{D}^{\mathrm{i}}, \tag{1}$$

where the elastic strain rate $\mathbf{D}^{\mathrm{e}}$ is given by

$$\mathbf{D}^{\mathrm{e}} = \mathbf{E}^{-1}\overset{\circ}{\boldsymbol{\sigma}}. \tag{2}$$

$\boldsymbol{\sigma}$ is the Cauchy stress and $(\circ)$ indicates the proper corotational rate with the objectivity and the fourth-order tensor $\mathbf{E}$ is the elastic modulus. Further, let the inelastic strain rate $\mathbf{D}^{\mathrm{i}}$ be additively decomposed into the *normal-plastic strain rate* $\mathbf{D}^{\mathrm{p}}_{\mathrm{n}}$ and the *tangential-plastic strain rate* $\mathbf{D}^{\mathrm{p}}_{\mathrm{t}}$ which are induced by the normal and tangential stress rate components, respectively, to the subloading surface, called the *normal* and *tangential stress rates*, respectively, i.e.

$$\mathbf{D}^{\mathrm{i}} = \mathbf{D}^{\mathrm{p}}_{\mathrm{n}} + \mathbf{D}^{\mathrm{p}}_{\mathrm{t}}. \tag{3}$$

Here, it is assumed that the tangential stress rate component inducing the tangential-plastic strain rate $\mathbf{D}^{\mathrm{p}}_{\mathrm{t}}$ is deviatoric stress, obeying the Rudnicki and Rice's (1975) conclusion that "no vertex can result from hydrostatic stress increments" based on the consideration of the sliding mechanism in the fissure model. Let $\mathbf{D}^{\mathrm{p}}_{\mathrm{n}}$ and $\mathbf{D}^{\mathrm{p}}_{\mathrm{t}}$ be formulated in this section.

Let it be postulated that the normal-plastic strain rate is given by the subloading surface model with the *smooth elastic-plastic transition* (Hashiguchi, 1980). Now, this model will be reviewed briefly.

Assume the yield condition:

$$f(\boldsymbol{\sigma}) = F(H). \tag{4}$$

The scalar H is the isotropic hardening/softening variable. Let it be assumed that the function f is homogeneous to degree one in the tensor $\boldsymbol{\sigma}$ satisfying $f(s\boldsymbol{\sigma}) = sf(\boldsymbol{\sigma})$ for any nonnegative scalar s. Here, assume that the evolution of the internal structure of materials is caused by the normal-plastic strain rate $\mathbf{D}^{\mathrm{p}}_{\mathrm{n}}$, and thus the evolution equation of H is homogeneous to degree one in $\mathbf{D}^{\mathrm{p}}_{\mathrm{n}}$. Then, assume that it is linear function of $\mathbf{D}^{\mathrm{p}}_{\mathrm{n}}$, i.e.

$$\overset{\bullet}{H} = \mathrm{tr}\{\mathbf{f}_h(\boldsymbol{\sigma}, H)\mathbf{D}^{\mathrm{p}}_{\mathrm{n}}\}, \tag{5}$$

where $\mathbf{f}_h$ is the second-order tensor, $(\bullet)$ stands for the material-time derivative and tr( ) is the trace.

Hereafter, the elastoplastic constitutive equation will be formulated in the framework of *unconventional plasticity* (Hashiguchi et al., 2002) as the extended plasticity theory such that the interior of the yield surface is not a purely elastic domain, but a plastic deformation is induced by the rate of stress inside the yield surface. Thus, the conventional yield surface is renamed as the *normal-yield surface*, since its interior is not regarded as a purely elastic domain in the present model.

Now, let the *subloading surface* be introduced, which always passes through the current stress point $\boldsymbol{\sigma}$ and also keeps the similar shape and the configuration of similarity to the normal-yield surface with respect to the origin of stress space, i.e. $\boldsymbol{\sigma} = \mathbf{0}$. The approaching degree to the normal-yield state can be described by the ratio of the size of the subloading surface to that of the normal-yield surface, i.e. the similarity-ratio R of these surfaces, while $R = 0$ corresponds to the most elastic state in which the stress coincides with the similarity-center and $R = 1$ to the normal-yield state in which the stress exists on the normal-yield surface. Hereinafter, the similarity-ratio R is called *the normal-yield ratio*. Then, the subloading surface is described as

$$f(\boldsymbol{\sigma}) = RF(H). \tag{6}$$

The normal-yield and subloading surfaces are illustrated in Fig. 1, where $\boldsymbol{\sigma}_y$ $(= \boldsymbol{\sigma}/R)$ on the normal-yield surface is the *conjugate stress* of the current stress $\boldsymbol{\sigma}$ on the subloading surface.

It is observed from experiments that the stress asymptotically approaches the normal-yield surface in the plastic loading process $\mathbf{D}^{\mathrm{p}}_{\mathrm{n}} \neq \mathbf{0}$. Thus, the following evolution equation of the normal-yield ratio R be assumed.

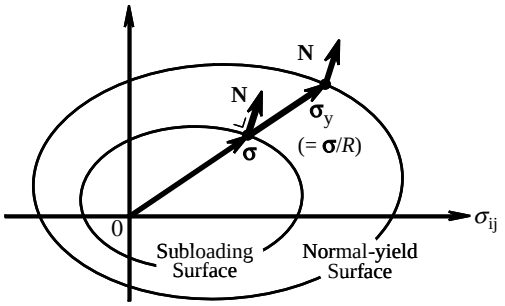

Fig. 1. Normal-yield and subloading surfaces.

$$\dot{R} = U\|\mathbf{D}_{\mathrm{n}}^{\mathrm{p}}\| \quad \text{for } \mathbf{D}_{\mathrm{n}}^{\mathrm{p}} \neq \mathbf{0}. \tag{7}$$

Here, $\|\ \|$ stands for the magnitude and U is the monotonically decreasing function of the normal-yield ratio R, satisfying

$$U = \begin{cases} \infty & \text{for} \quad R = 0, \\ 0 & \text{for} \quad R = 1, \end{cases} \quad (U < 0 \quad \text{for } R > 1), \tag{8}$$

where the fact that the stress increases without a plastic strain rate at the most elastic state $R = 0$ is incorporated. The function U satisfying Eq. (8) be simply given by

$$U = -u_R \ln R, \tag{9}$$

where u_R is a material constant prescribing the approaching rate of the current stress to the normal-yield surface with a plastic deformation.

Assuming the associated flow rule:

$$\mathbf{D}_{\mathrm{n}}^{\mathrm{p}} = \lambda \mathbf{N} (\lambda > 0), \tag{10}$$

where

$$\lambda = \frac{\mathrm{tr}(\mathbf{N}\overset{\circ}{\boldsymbol{\sigma}})}{M_{\mathrm{n}}^{\mathrm{p}}}, \tag{11}$$

$$\mathbf{N} \equiv \frac{\partial f(\boldsymbol{\sigma})}{\partial \boldsymbol{\sigma}} \Big/ \left\| \frac{\partial f(\boldsymbol{\sigma})}{\partial \boldsymbol{\sigma}} \right\| \quad (\|\mathbf{N}\| = 1), \tag{12}$$

$$M_{\mathrm{n}}^{\mathrm{p}} \equiv \left(\frac{F'}{F} h + \frac{U}{R} \right) \mathrm{tr}(\mathbf{N}\boldsymbol{\sigma}), \tag{13}$$

where $M_{\mathrm{n}}^{\mathrm{p}}$ is called *normal-plastic modulus* and h is a function of the stress, plastic internal variables and $\mathbf{N}$ in degree one, which is related to $\dot{H}$ as

$$h \equiv \mathrm{tr}(\mathbf{f}_h \mathbf{N}) = \frac{\dot{H}}{\lambda}, \tag{14}$$

since the rates of internal variables include λ in degree one.

The normal-plastic strain rate (10) with Eqs. (11) and (13) is obtained by substituting the associated flow rule (10) into the extended consistency condition obtained by incorporating the evolution rule (7) of the normal-yield ratio R into the time-differentiation of Eq. (6) for the subloading surface. Then, the plastic

loading process develops gradually as the stress approaches the normal-yield surface, exhibiting a *smooth elastic–plastic transition*. Thus, the subloading surface model fulfills the *smoothness condition* (Hashiguchi, 1993b, 1997, 2000).

Noting that the tangential-plastic strain rate $\mathbf{D}_{\mathrm{t}}^{\mathrm{p}}$, as well as the normal-plastic strain rate $\mathbf{D}_{\mathrm{n}}^{\mathrm{p}}$, would not be induced in the state $R=0$, but would be gradually induced as the stress approaches the normal-yield surface, let the tangential-plastic strain rate $\mathbf{D}_{\mathrm{t}}^{\mathrm{p}}$ be formulated as

$$\mathbf{D}_{\mathrm{t}}^{\mathrm{p}}=\frac{1}{M_{\mathrm{t}}^{\mathrm{p}}}\overset{\circ}{\boldsymbol{\sigma}}{}_{\mathrm{t}}^{*}, \tag{15}$$

where $M_{\mathrm{t}}^{\mathrm{p}}$ is a monotonically decreasing function of R satisfying the following conditions.

$$M_{\mathrm{t}}^{\mathrm{p}}=\begin{cases}\infty & \text{for } R=0,\\ T & \text{for } R=1.\end{cases} \tag{16}$$

T being a material function of the stress and the plastic internal variables in general. The function $M_{\mathrm{t}}^{\mathrm{p}}$, called the *tangential-plastic modulus*, satisfying Eq. (16) is simply given by

$$M_{\mathrm{t}}^{\mathrm{p}}=TR^{-b}, \tag{17}$$

where b ($\geqslant 1$) is a material constant. The second-order tensor $\overset{\circ}{\boldsymbol{\sigma}}{}_{\mathrm{t}}^{*}$ is given as follows:

$$\overset{\circ}{\boldsymbol{\sigma}}{}_{\mathrm{t}}^{*}\equiv\overset{\circ}{\boldsymbol{\sigma}}{}^{*}-\overset{\circ}{\boldsymbol{\sigma}}{}_{\mathrm{n}}^{*},\quad \overset{\circ}{\boldsymbol{\sigma}}{}_{\mathrm{n}}^{*}\equiv\mathrm{tr}(\mathbf{n}^{*}\overset{\circ}{\boldsymbol{\sigma}}{}^{*})\mathbf{n}^{*}, \tag{18}$$

$$\mathbf{n}^{*}\equiv\left(\frac{\partial f(\boldsymbol{\sigma})}{\partial\boldsymbol{\sigma}}\right)^{*}\Big/\left\|\left(\frac{\partial f(\boldsymbol{\sigma})}{\partial\boldsymbol{\sigma}}\right)^{*}\right\|\quad(\|\mathbf{n}^{*}\|=1). \tag{19}$$

$(\ )^{*}$ stands for the deviatoric part and $\mathbf{n}^{*}$ is the normalized deviatoric outward-normal tensor of the subloading surface. The stress rate $\overset{\circ}{\boldsymbol{\sigma}}{}_{\mathrm{t}}^{*}$ is called the *deviatoric tangential stress rate* fulfilling

$$\mathrm{tr}(\mathbf{N}\overset{\circ}{\boldsymbol{\sigma}}{}_{\mathrm{t}}^{*})=0,\quad \mathrm{tr}(\overset{\circ}{\boldsymbol{\sigma}}{}_{\mathrm{t}}^{*})=0. \tag{20}$$

The deviatoric tangential stress rate $\overset{\circ}{\boldsymbol{\sigma}}{}_{\mathrm{t}}^{*}$ in the principal stress space is directed toward the tangential line of the closed curve formed by the intersection of the subloading surface and deviatoric stress plane as illustrated in Fig. 2. The tangential-plastic strain rate $\mathbf{D}_{\mathrm{t}}^{\mathrm{p}}$ is related linearly to the deviatoric-tangential stress rate $\overset{\circ}{\boldsymbol{\sigma}}{}_{\mathrm{t}}^{*}$ through the similarity-ratio R so as to exhibit the smooth elastic–inelastic transition. Besides, it can be formulated so as to be hardly induced when a stress lies inside the normal-yield surface by giving a large value to the material parameter b.

The strain rate $\mathbf{D}$ is given as

$$\mathbf{D}=\mathbf{E}^{-1}\overset{\circ}{\boldsymbol{\sigma}}+\frac{\mathrm{tr}(\mathbf{N}\overset{\circ}{\boldsymbol{\sigma}})}{M_{\mathrm{n}}^{\mathrm{p}}}\mathbf{N}+\frac{1}{M_{\mathrm{t}}^{\mathrm{p}}}\overset{\circ}{\boldsymbol{\sigma}}{}_{\mathrm{t}}^{*}. \tag{21}$$

Now, let the elastic modulus tensor $\mathbf{E}$ be given by the Hooke's type as

$$E_{ijkl}=\left(K-\frac{2}{3}G\right)\delta_{ij}\delta_{kl}+G(\delta_{ik}\delta_{jl}+\delta_{il}\delta_{jk}), \tag{22}$$

where K and G are the elastic bulk and shear moduli, respectively, which are functions of the stress and internal state variables in general and δ_{ij} is the Kronecker's delta. The inverse expression of Eq. (21) is given as

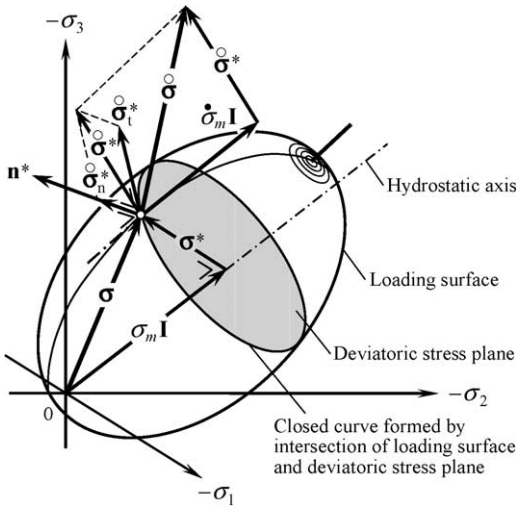

Fig. 2. The deviatoric tangential stress rate $\overset{\circ}{\boldsymbol{\sigma}}{}^*_{\mathrm{t}}$ illustrated in the principal stress space.

$$\overset{\circ}{\boldsymbol{\sigma}} = \frac{M^{\mathrm{p}}_{\mathrm{t}}}{M^{\mathrm{p}}_{\mathrm{t}} + 2G}\left[\mathbf{ED} - \frac{\mathrm{tr}(\mathbf{NED})}{M^{\mathrm{p}}_{\mathrm{n}} + \mathrm{tr}(\mathbf{NEN})}\left\{\mathbf{EN} + \frac{2G}{M^{\mathrm{p}}_{\mathrm{t}}}(\mathrm{tr}(\mathbf{n}^*\mathbf{EN})\mathbf{n}^* + \frac{1}{3}\mathrm{tr}(\mathbf{EN})\mathbf{I})\right\}\right.$$
$$\left. + \frac{2G}{M^{\mathrm{p}}_{\mathrm{t}}}(\mathrm{tr}(\mathbf{n}^*\mathbf{ED})\mathbf{n}^* + \frac{1}{3}\mathrm{tr}(\mathbf{ED})\mathbf{I})\right]. \tag{23}$$

The positive proportionality factor in the associated flow rule is expressed in terms of the strain rate $\mathbf{D}$, rewriting λ by Λ, as follows:

$$\Lambda = \frac{\mathrm{tr}(\mathbf{NED})}{M^{\mathrm{p}}_{\mathrm{n}} + \mathrm{tr}(\mathbf{NEN})} \tag{24}$$

because of $\mathrm{tr}(\mathbf{NE}\overset{\circ}{\boldsymbol{\sigma}}{}^*_{\mathrm{t}}) = 0$ for Eq. (22). Then, let the loading criterion be given by the positiveness of the proportionality factor Λ as follows (Hashiguchi, 2000):

$$\left.\begin{array}{l}\mathbf{D}^{\mathrm{p}}_{\mathrm{n}} \neq \mathbf{0} : \Lambda > 0, \\ \mathbf{D}^{\mathrm{p}}_{\mathrm{n}} = \mathbf{0} : \Lambda \leqslant 0.\end{array}\right\} \tag{25}$$

3. Material functions for soils

The particular forms of the material functions for soils are given in this section. We focus our attention on the behavior of saturated soils, and then let the *Cauchy stress* tensor $\boldsymbol{\sigma}$ be meant the *effective Cauchy stress*, excluding a pore pressure u from the *total Cauchy stress* $\mathbf{T}$, which is defined by

$$\boldsymbol{\sigma} = \mathbf{T} + u\mathbf{I}. \tag{26}$$

where u as well as pressure p_σ $(\equiv -\sigma_m)$ is taken to be positive for compression.

The subloading surface for simple isotropic soils is given as follows:

$$f(\boldsymbol{\sigma}) = p_\sigma(1 + \chi^2), \tag{27}$$

where

$$p_\sigma \equiv -\frac{1}{3}\mathrm{tr}\,\boldsymbol{\sigma}, \quad \chi \equiv \frac{\|\boldsymbol{\eta}\|}{m_\mathrm{c}}, \tag{28}$$

$$\boldsymbol{\eta} \equiv \frac{\boldsymbol{\sigma}^*}{p_\sigma}, \quad \boldsymbol{\sigma}^* \equiv \boldsymbol{\sigma} + p_\sigma \mathbf{I}. \tag{29}$$

m_c is the material constant describing the stress ratio $\|\boldsymbol{\eta}\|$ in the critical state line.

The isotropic hardening/softening function F is given by

$$F = F_0 \exp\left(\frac{H}{\rho - \gamma}\right), \tag{30}$$

where F_0 is the initial value of F. ρ and γ are material constants describing the slope of the normal consolidated curve and the swelling curve, respectively, in the $(\ln V, \ln P)$ plane (V: volume, P: pressure). The evolution equation of the isotropic hardening variable H is given by

$$\overset{\bullet}{H} = -\mathrm{tr}(\mathbf{D}_\mathrm{n}^\mathrm{p}). \tag{31}$$

Further, we assume the function T in the tangential-plastic modulus M_t^p of Eq. (17) as

$$T = \frac{p_\sigma}{a\chi^c}, \tag{32}$$

a and c are material constants. Then, the tangential-plastic modulus M_t^p in Eq. (15) with Eqs. (17) and (32) is formulated to induce the tangential stress rate effect gradually with the increase in χ and/or R, whilst the effect decreases with the increase in pressure. On the other hand, the equation of Yatomi et al. (1989) for the tangential-plastic modulus, i.e. $M_\mathrm{t}^\mathrm{p} = C(m_c - \|\boldsymbol{\eta}\|)p_\sigma$ (C: material constant) is applicable only to the normal-yield state $R = 1$ under a lower stress ratio than that in the critical state, i.e. $\chi \leqslant 1$.

The bulk and shear moduli are given as

$$K = \frac{p_\sigma}{\gamma}, \quad G = \frac{3(1-2\nu)}{2(1+\nu)}K, \tag{33}$$

where ν is Poisson's ratio.

The concrete form of the normal-plastic modulus in Eq. (13) for isotropic soils is described from Eqs. (27)–(30) as follows:

$$\left.\begin{aligned} M_\mathrm{n}^\mathrm{p} &= \left(-u_R \ln R + \frac{R}{\rho-\gamma}\frac{1-\chi^2}{\sqrt{\varsigma}}\right)\frac{F}{\sqrt{\varsigma}}, \\ \varsigma &\equiv \tfrac{1}{3}(1-\chi^2)^2 + \left(2\frac{\chi}{m_c}\right)^2. \end{aligned}\right\} \tag{34}$$

Hereafter, the material constants are chosen as $\rho = 0.0924$, $\gamma = 0.0168$, $m_c = 1.17$, $b = 1.0$, $c = 3.0$ and $\nu = 0.333$.

4. Constitutive relations

Consider a soil specimen in the shape of a rectangular and homogeneous block under the plane strain deformations subjected to continuing biaxial loading of homogeneous normal stress in the (x_1, x_3) plane as the current axial compressive stress σ_{11} on the frictionless ends and the lateral compressive stress σ_{33} on the

sides, which starts from an isotropically consolidated state (see Fig. 3). At the onset of deformation, we suppose the specimen undergoes a finite homogenous deformation and the pore water pressure maintains homogeneous. Furthermore, the deformed specimen preserves a rectangular shape with the current dimensions $2a_1 \times 2a_3$ at the onset of bifurcation. The shear band, symmetric and anti-symmetric modes may be induced as shown in Fig. 3. Considering the constitutive relationship (23), it holds that

$$\left.\begin{aligned} \overset{\circ}{\sigma}_{11} - \overset{\circ}{\sigma}_{33} &= 2\mu^*(D_{11} - D_{33}), \\ \overset{\circ}{\sigma}_{31} &= 2\mu D_{31}, \end{aligned}\right\} \tag{35}$$

with

$$D_{11} + D_{33} = 0, \quad D_{12} = D_{22} = D_{23} = 0. \tag{36}$$

μ^* and μ which are the instantaneous shear moduli for the normal effective stress difference $\sigma_{11} - \sigma_{33}$ and for shear stress σ_{31}, respectively are derived as follows (Hashiguchi and Tsutsumi, 2003):

$$\mu^* = G\frac{M_{\mathrm{n}}^{\mathrm{r}}}{M_{\mathrm{n}}^{\mathrm{e}}}(\leqslant G), \tag{37}$$

$$\mu = G\frac{M_{\mathrm{t}}^{\mathrm{p}}}{M_{\mathrm{t}}^{\mathrm{p}} + 2G}(\leqslant G), \tag{38}$$

where

$$M_{\mathrm{n}}^{\mathrm{r}} \equiv M_{\mathrm{n}}^{\mathrm{p}} + \frac{K}{\varsigma}(1-\chi^2)^2, \quad M_{\mathrm{n}}^{\mathrm{e}} \equiv M_{\mathrm{n}}^{\mathrm{p}} + \frac{1}{\varsigma}\left(K - \frac{2}{3}G\right)(1-\chi^2)^2 + 2G. \tag{39}$$

Further, for biaxial loading under the undrained plane strain conditions starting from the isotropic-consolidation state, the following simple relationship can be obtained.

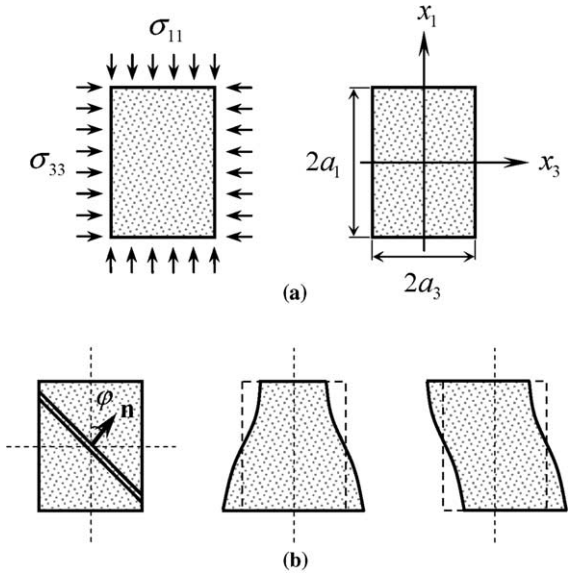

Fig. 3. (a) The boundary stresses at the onset of bifurcation and the geometric configuration. (b) The localized bifurcation mode (shear band) and the diffuse bifurcation modes (bulging and buckling).

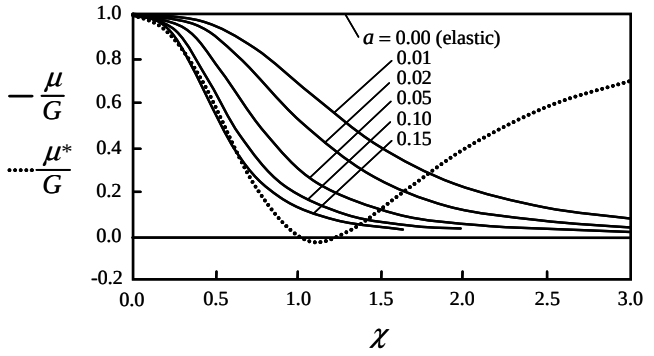

Fig. 4. Relationships of the instantaneous shear moduli vs. the variable χ with the variation of the material parameter a in the normal-yield state ($R = 1$).

$$\frac{1}{2}(\sigma_{11} - \sigma_{33}) = \frac{\sqrt{2}}{2} m_c p_\sigma \chi. \tag{40}$$

The instantaneous shear modulus μ^* in Eq. (37) is independent of the tangential-plastic strain rate and gradually decreases from the elastic shear modulus G as χ and R increase, as shown in Fig. 4, for the normal-yield state $R = 1$ and in Fig. 5 for $u_R = 10$, whilst it increases inversely in the regime far denser than

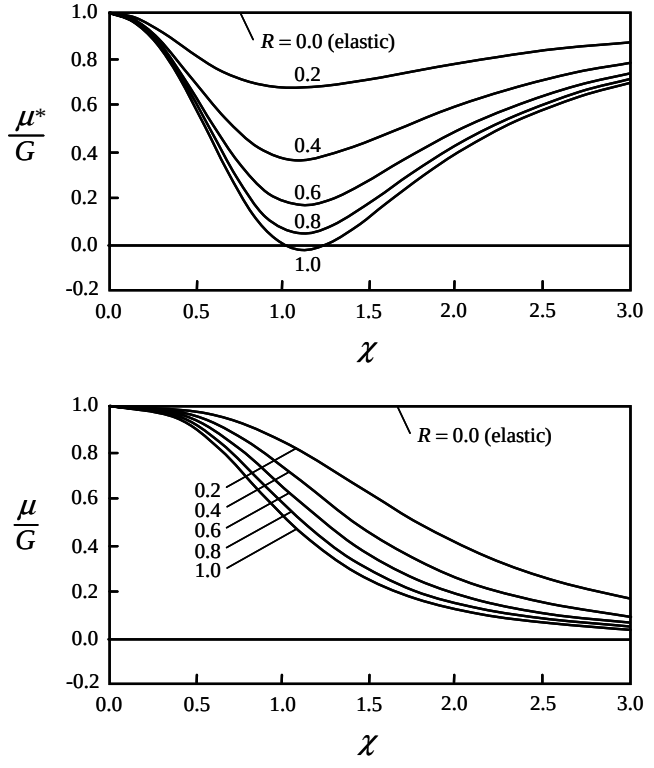

Fig. 5. Relationships of the instantaneous shear moduli vs. the variable χ with the variation of the normal-yield ratio R for $u_R = 10$ and $a = 0.02$.

critical state ($\chi \gg 1$ and $M_{\mathrm{n}}^{\mathrm{p}} < 0$). Note that μ^* is slightly negative near the normal-yield state and just over the critical state.

The instantaneous shear modulus μ in Eq. (38) decreases monotonically with the increase in the value of the material parameter a and with the increase in the variables χ and R, as shown in Figs. 4 and 5.

The feature of the present formulation where the tangential-plastic strain rate, as well as the normal-plastic strain rate, is induced gradually as the stress approaches the normal-yield surface, i.e. as $R \to 1$, fulfilling both the continuity and smoothness conditions is shown in Figs. 4 and 5. On the other hand, in conventional plasticity models with $a = 0$, μ^* and μ suddenly jump from the purely elastic response to the normal-yield response at the moment when the stress reaches the normal-yield surface.

5. Governing equations

At the current time t, let the body be bounded by closed surface s and let $\mathbf{t}$ denote the surface traction vector. Then, it is required to satisfy

$$\int_s \mathbf{t}\,\mathrm{d}s = 0 \tag{41}$$

for equilibrium without the body force. Using the divergence theorem and the relation $\mathbf{t} = \mathbf{T}\mathbf{n}$ ($\mathbf{n}$: the outward unit normal to the surface s), we obtain the equilibrium equation

$$\mathrm{div}\,\mathbf{T} = 0. \tag{42}$$

Noting that $(\mathrm{d}s)^{\bullet} = (\mathrm{tr}\,\mathbf{D} - \mathbf{n}\cdot\mathbf{D}\mathbf{n})\,\mathrm{d}s$, the differentiation of Eq. (41) with respect to time is given by

$$\int_s \dot{\boldsymbol{\pi}}\,\mathrm{d}s = 0, \tag{43}$$

where $\dot{\boldsymbol{\pi}} = \dot{\mathbf{t}} + (\mathrm{tr}\,\mathbf{D} - \mathbf{n}\cdot\mathbf{D}\mathbf{n})\mathbf{t}$ is called the *total nominal traction rate*. Further, the *total nominal* (*first Piola–Kirchhoff*) *stress rate* $\dot{\boldsymbol{\Pi}}$ defined by $\dot{\boldsymbol{\pi}} = \dot{\boldsymbol{\Pi}}\mathbf{n}$ is related to the *total Cauchy stress rate* $\dot{\mathbf{T}}$ by

$$\dot{\boldsymbol{\Pi}} = \dot{\mathbf{T}} + (\mathrm{tr}\,\mathbf{D})\mathbf{T} - \mathbf{T}\mathbf{L}^{\mathrm{T}}. \tag{44}$$

Since the stress rates $\dot{\mathbf{T}}$ and $\dot{\boldsymbol{\sigma}}$ are not invariant under rigid rotation, let the corresponding *Jaumann rate* be introduced as the objective corotational rates:

$$\overset{\circ}{\mathbf{T}} \equiv \dot{\mathbf{T}} + \mathbf{T}\mathbf{W} - \mathbf{W}\mathbf{T}, \tag{45}$$

$$\overset{\circ}{\boldsymbol{\sigma}} \equiv \dot{\boldsymbol{\sigma}} + \boldsymbol{\sigma}\mathbf{W} - \mathbf{W}\boldsymbol{\sigma}. \tag{46}$$

Substituting Eqs. (45) and (46) to Eq. (44) with Eq. (26), the total nominal stress rate $\dot{\boldsymbol{\Pi}}$ can be rewritten as

$$\dot{\boldsymbol{\Pi}} = \overset{\circ}{\mathbf{T}} + (\mathrm{tr}\,\mathbf{D})\mathbf{T} - \mathbf{T}\mathbf{D} + \mathbf{W}\mathbf{T} = \dot{\boldsymbol{\Pi}}' - \dot{u}\mathbf{I} - u(\mathrm{tr}\,\mathbf{D})\mathbf{I} + u\mathbf{L}^{\mathrm{T}}, \tag{47}$$

where

$$\dot{\boldsymbol{\Pi}}' = \overset{\circ}{\boldsymbol{\sigma}} + (\mathrm{tr}\,\mathbf{D})\boldsymbol{\sigma} - \boldsymbol{\sigma}\mathbf{D} + \mathbf{W}\boldsymbol{\sigma}. \tag{48}$$

$\dot{\boldsymbol{\Pi}}'$ is called the *effective nominal stress rate* (Yatomi et al., 1989).

Using the divergence theorem in Eq. (43), the equilibrium equation is obtained as

$$\mathrm{div}\,\dot{\boldsymbol{\Pi}}' - \mathrm{grad}\,\dot{u} = 0. \tag{49}$$

for $\mathrm{grad}\,u = 0$.

For the plane strain deformation, the rate of deformation tensor $\mathbf{D}$ and the spin tensor $\mathbf{W}$ are given by

$$\mathbf{D}=\begin{bmatrix} \dfrac{\partial v_1}{\partial x_1} & \dfrac{1}{2}\left(\dfrac{\partial v_1}{\partial x_3}+\dfrac{\partial v_3}{\partial x_1}\right) \\ \dfrac{1}{2}\left(\dfrac{\partial v_1}{\partial x_3}+\dfrac{\partial v_3}{\partial x_1}\right) & \dfrac{\partial v_3}{\partial x_3} \end{bmatrix}, \tag{50}$$

$$\mathbf{W}=\begin{bmatrix} 0 & \dfrac{1}{2}\left(\dfrac{\partial v_1}{\partial x_3}-\dfrac{\partial v_3}{\partial x_1}\right) \\ -\dfrac{1}{2}\left(\dfrac{\partial v_1}{\partial x_3}-\dfrac{\partial v_3}{\partial x_1}\right) & 0 \end{bmatrix}. \tag{51}$$

In addition, using the relationships between the Jaumann rate and the material time rate of Cauchy stress, Eq. (46), and between the effective nominal stress rate $\dot{\mathbf{\Pi}}'$ and the Jaumann rate of Cauchy stress $\overset{\circ}{\boldsymbol{\sigma}}$, Eq. (48), the following equations are obtained, respectively:

$$\overset{\circ}{\boldsymbol{\sigma}}=\begin{bmatrix} \dot{\sigma}_{11} & \dot{\sigma}_{13}+\tau\left(\dfrac{\partial v_1}{\partial x_3}-\dfrac{\partial v_3}{\partial x_1}\right) \\ \dot{\sigma}_{31}+\tau\left(\dfrac{\partial v_1}{\partial x_3}-\dfrac{\partial v_3}{\partial x_1}\right) & \dot{\sigma}_{33} \end{bmatrix}, \tag{52}$$

$$\dot{\mathbf{\Pi}}'=\begin{bmatrix} \overset{\circ}{\sigma}_{11}-\sigma_{11}\dfrac{\partial v_1}{\partial x_1} & \overset{\circ}{\sigma}_{13}-\tau\dfrac{\partial v_1}{\partial x_3}-\sigma\dfrac{\partial v_3}{\partial x_1} \\ \overset{\circ}{\sigma}_{31}-\sigma\dfrac{\partial v_1}{\partial x_3}+\tau\dfrac{\partial v_3}{\partial x_1} & \overset{\circ}{\sigma}_{33}-\sigma_{33}\dfrac{\partial v_3}{\partial x_3} \end{bmatrix}, \tag{53}$$

where

$$\sigma=\frac{1}{2}(\sigma_{11}+\sigma_{33}),\quad \tau=\frac{1}{2}(\sigma_{11}-\sigma_{33}). \tag{54}$$

Let the bifurcation condition in the biaxial compressive loading under the undrained condition be analyzed, as established by Hill and Hutchinson (1975) for plastically-incompressible metals and followed by Young (1976), Needleman (1979), Vardoulakis (1981), Chau and Rudnicki (1990) and Bardet (1991). Consider a pure homogeneous deformation process which starts from an isotropically consolidated state and proceeds up to the instant of the bifurcation phenomena, where the principal stress axes coincide with the directions of the coordinate axes x_1 and x_3. On the ends $(x_1=\pm a_1)$,the specimen is loaded by a compressive velocity with no shear traction and on the side $(x_3=\pm a_3)$, a constant lateral hydrostatic pressure. Using Eq. (49) for continuing linear equilibrium, the total nominal stress rate must satisfy

$$\left.\begin{aligned} \frac{\partial \dot{\Pi}'_{11}}{\partial x_1}+\frac{\partial \dot{\Pi}'_{13}}{\partial x_3}-\frac{\partial \dot{u}}{\partial x_1}=0, \\ \frac{\partial \dot{\Pi}'_{33}}{\partial x_3}+\frac{\partial \dot{\Pi}'_{31}}{\partial x_1}-\frac{\dot{u}}{\partial x_3}=0. \end{aligned}\right\} \tag{55}$$

Eq. (55) can be written as follows:

$$\left.\begin{aligned} \frac{\partial}{\partial x_1}(\dot{\Pi}'_{11}-\dot{\Pi}'_{33})+2\frac{\partial}{\partial x_3}\dot{\Pi}'_{13}-2\frac{\partial}{\partial x_1}\dot{u}=-\frac{\partial}{\partial x_1}(\dot{\Pi}'_{11}+\dot{\Pi}'_{33}), \\ \frac{\partial}{\partial x_3}(\dot{\Pi}'_{11}-\dot{\Pi}'_{33})-2\frac{\partial}{\partial x_1}\dot{\Pi}'_{31}+2\frac{\partial}{\partial x_3}\dot{u}=\frac{\partial}{\partial x_3}(\dot{\Pi}'_{11}+\dot{\Pi}'_{33}). \end{aligned}\right\} \tag{56}$$

Differentiating and combining the two relationships in Eq. (56) to eliminate $\overset{\bullet}{\Pi}'_{11} + \overset{\bullet}{\Pi}'_{33}$, the resulting can be expressed in terms of the derivatives of velocities using Eq. (53). Then, introduce the stream function $\Psi(x_1, x_3)$(Hill and Hutchinson, 1975) leading to

$$v_1 = \frac{\partial \Psi}{\partial x_3}, \quad v_3 = \frac{\partial \Psi}{\partial x_1}. \tag{57}$$

The substitution of Eqs. (53) and (57) into Eq. (56) with constitutive relations (35) leads to

$$(\mu - \tau)\frac{\partial^4 \Psi}{\partial x_3^4} + 2(2\mu^* - \mu)\frac{\partial^4 \Psi}{\partial x_1^2 \partial x_3^2} + (\mu + \tau)\frac{\partial^4 \Psi}{\partial x_1^4} = 0. \tag{58}$$

Eq. (58) is a fourth order partial differential equation of the mixed type that can be elliptic, hyperbolic or parabolic, depending on the current state of stress and internal variables. The particular linearization described here yields a governing equation by applying subloading surface model with tangential stress rate effect.

6. Localized bifurcation and classification of regimes

The condition of shear band formation at the onset of strain localization in the biaxial compressive loading under the undrained conditions is analyzed briefly in this section. The unit vector normal to a shear band is denoted by $\mathbf{n}(n_1, n_3)$ (see Fig. 3). The stream function $\Psi(x_1, x_3)$, which represents a simple shear parallel to planes $n_1 x_1 + n_3 x_3 = \text{const.}$, is given by

$$\Psi = \Psi(n_1 x_1 + n_3 x_3). \tag{59}$$

The substitution of Eq. (59) into (58) gives a fourth order algebraic characteristic equation as follows:

$$(\mu - \tau)n_3^4 + 2(2\mu^* - \mu)n_1^2 n_3^2 + (\mu + \tau)n_1^4 = 0. \tag{60}$$

The condition for the formation of shear band is given as a loss of ellipticity of Eq. (60), whilst the solutions of n_3/n_1 in Eq. (60) are classified into the elliptic complex (EC) and imaginary (EI), parabolic (P) and hyperbolic (H) regimes, according to the existence of zero, two, and four real roots for (60), respectively. The classifications of the regimes, under the restrictions $\mu^* > 0$, $\mu > 0$ and $\tau > 0$, are as follows:

Elliptic complex regime:

$$\frac{\mu}{2\mu^*} > \frac{1}{2}\left(\frac{\tau}{2\mu^*}\right)^2 + \frac{1}{2}. \tag{61}$$

Elliptic imaginary regime:

$$\frac{\mu}{2\mu^*} < \frac{1}{2}\left(\frac{\tau}{2\mu^*}\right)^2 + \frac{1}{2}, \quad \mu > \tau, \quad 2\mu^* > \mu. \tag{62}$$

Parabolic regime:

$$\mu < \tau. \tag{63}$$

Hyperbolic regime:

$$\frac{\mu}{2\mu^*} < \frac{1}{2}\left(\frac{\tau}{2\mu^*}\right)^2 + \frac{1}{2}, \quad \mu > \tau, \quad 2\mu^* < \mu. \tag{64}$$

The boundaries between the characteristic regimes are classified as follows:

Elliptic complex–elliptic imaginary boundary:

$$\left.\begin{array}{l} 2\mu^* > \mu, \\ \left(\dfrac{n_3}{n_1}\right)_{1,2,3,4} = \pm \mathrm{i}\left(\dfrac{2\mu^* - \mu}{\mu - \tau}\right)^{1/2}, \quad \mathrm{i} = \sqrt{-1}. \end{array}\right\} \tag{65}$$

Elliptic complex–hyperbolic boundary:

$$\left.\begin{array}{l} 2\mu^* < \mu, \\ \left(\dfrac{n_3}{n_1}\right)_{1,2,3,4} = \pm\left(-\dfrac{2\mu^* - \mu}{\mu - \tau}\right)^{1/2}. \end{array}\right\} \tag{66}$$

Elliptic–parabolic boundary:

$$\left.\begin{array}{l} 2\mu^* > \mu, \\ \left(\dfrac{n_3}{n_1}\right)_{1,2} = 0, \quad \left(\dfrac{n_3}{n_1}\right)_{3,4} = \pm \mathrm{i}\left(2\dfrac{2\mu^* - \mu}{\mu - \tau}\right)^{1/2}. \end{array}\right\} \tag{67}$$

Hyperbolic–parabolic boundary:

$$\left.\begin{array}{l} 2\mu^* < \mu, \\ \left(\dfrac{n_3}{n_1}\right)_{1,2} = 0, \quad \left(\dfrac{n_3}{n_1}\right)_{3,4} = \pm\left(-2\dfrac{2\mu^* - \mu}{\mu - \tau}\right)^{1/2}. \end{array}\right\} \tag{68}$$

Let it be assumed that the shear band will be formed at the instant when the $(\tau/2\mu^*, \mu/2\mu^*)$ trajectory passes through the EC–H boundary. Then, the inclination angle φ of shear band, i.e. the angle measured in anti-clockwise direction from the maximum principal stress (σ_{11}) direction to the direction of shear band (the direction normal to shear band) is given from Eq. (60) as

$$\varphi = \tan^{-1}\left(\frac{n_3}{n_1}\right) = \tan^{-1}\sqrt{-\frac{2\mu^* - \mu}{\mu - \tau}}. \tag{69}$$

Here, note that when the trajectory directly passes though the E–P boundary $(\mu = \tau, 2\mu^* > \mu)$ $n_1 = 0$ is derived from Eq. (60), and thus the direction of the shear band is unrealistically predicted perpendicular to the maximum principal stress direction, i.e. $\varphi = \pi/2$. Therefore, one would have only to consider the EC–H boundary for shear band formation.

The relationships between the inclination angle φ of shear band vs. $\tau/2\mu^*$ for several levels of material parameter a ranging from 0.1 to 0.55 are obtained from Eq. (69) and depicted in Fig. 6. The angle φ increases for a bigger material parameter a. In cases of a larger material parameter a, the inclination angle φ is predicted unrealistically as $\varphi > \pi/2$ since the trajectories directly pass though the E–P boundary.

The regions in the stress space where the shear band can be induced are depicted in Fig. 7 for three levels of the material parameter: (a) $u_R = 1$, (b) $u_R = 10$ and (c) $u_R = 100$. It is found that the lower material parameter u_R gives a wider region of stress for the shear band formation, inducing inelastic deformation from the lower value of R. It should be noted that the shear band is formed for a stress ratio lower than the critical state in the case of $R = 1$, but it is done even for stress ratios higher than the critical state in the case of $R < 1$, while the range of the stress inducing the shear band is affected by the material parameter u_R.

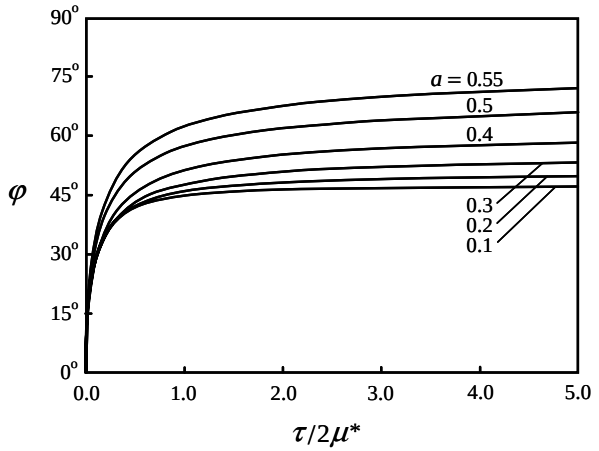

Fig. 6. Relationships of shear band inclination angle φ vs. $\tau/2\mu^*$ with the variation of material parameter a.

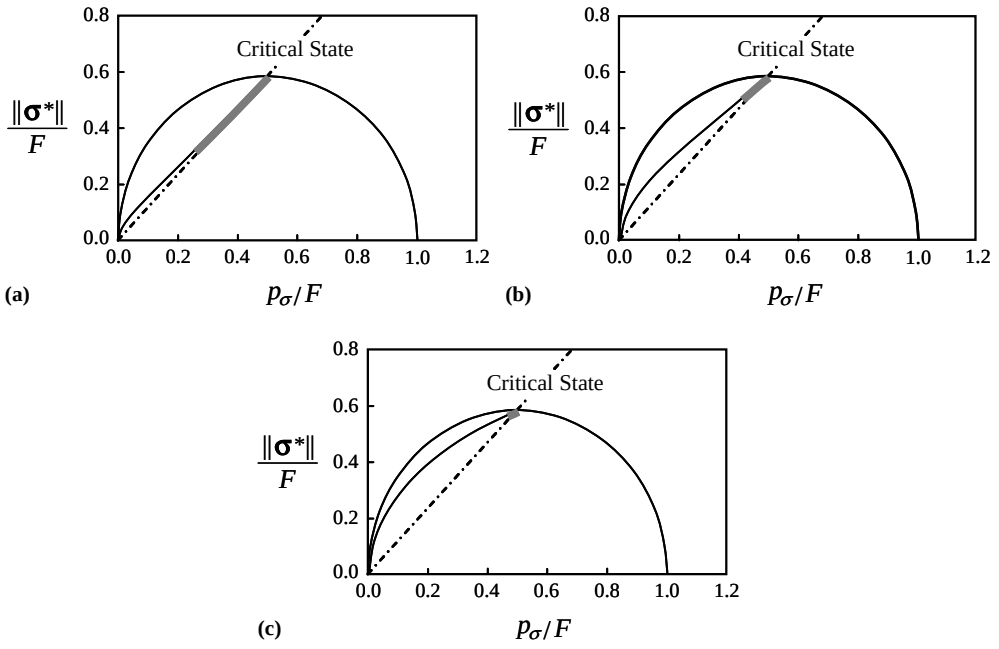

Fig. 7. Possible regions of shear band formation illustrated in the non-dimensional stress plane $(p_\sigma/F, \|\boldsymbol{\sigma}^*\|/F)$ for three levels of the material parameter u_R: (a) $u_R = 1$, (b) $u_R = 10$ and (c) $u_R = 100$.

7. Diffuse bifurcation modes and classification of regimes

In this section, we investigate the possibility of diffuse bifurcations, which precedes localization, for a rectangular soil specimen with the dimensions $2a_1 \times 2a_3$ at the onset of bifurcation (see Fig. 3). We examine the possibility of incremental deformation when the ends are subject to a current axial stress σ_{11} and the

sides subject to a constant hydrostatic confining pressure $\sigma_{11} = \sigma_c$. The stream function $\Psi(x_1, x_3)$, which represents the diffuse bifurcation modes is given by

$$\Psi(x_1, x_3) = v(x_3)\cos(\zeta x_1), \tag{70}$$

where $\zeta = m\pi/2a_1$, $m = 1, 2, 3, \ldots$. The substitution of Eq. (70) into Eq. (57) leads to

$$\left.\begin{aligned} v_1 &= v'(x_3)\cos(\zeta x_1), \\ v_3 &= \zeta v(x_3)\sin(\zeta x_1), \end{aligned}\right\} \tag{71}$$

where $v' = \mathrm{d}v_3/\mathrm{d}x_3$. Here, as in Hill and Hutchinson (1975), the origin of coordinates is at the rectangular specimen center when m is odd and at a distance a_1/m from the center when m is even. Substituting of the eigenmode (71) into Eq. (58), the following governing differential equation is obtained for $v(x_3)$.

$$(\mu - \tau)v'''' - 2(2\mu^* - \mu)\zeta^2 v'' + (\mu + \tau)\zeta^4 v = 0. \tag{72}$$

Noting that Eq. (47), the boundary conditions can be written

$$\left.\begin{aligned} &v_1 = 0, \quad \overset{\bullet}{\Pi}{}'_{31} = 0 && \text{on the ends,} \\ &\overset{\bullet}{\Pi}{}'_{33} = \overset{\bullet}{u} - \sigma_c \frac{\partial v_3}{\partial x_3}, \quad \overset{\bullet}{\Pi}{}'_{13} = -\sigma_c \frac{\partial v_3}{\partial x_1} && \text{on the sides.} \end{aligned}\right\} \tag{73}$$

Substituting Eq. (35), (36) and (73) into Eq. (55), the boundary conditions on the sides can be expressed

$$\left.\begin{aligned} &v'' + \zeta^2 v = 0, \\ &(\mu - \tau)v''' - (4\mu^* - \mu - \tau)\zeta^2 v' = 0 \end{aligned}\right\} \quad \text{on } x_3 = \pm a_3. \tag{74}$$

The symmetric modes satisfy $\Psi(x_1, x_3) = -\Psi(x_1, -x_3)$ based on odd functions $v(x_3)$ and the anti-symmetric modes satisfy $\Psi(x_1, x_3) = \Psi(x_1, -x_3)$ based on even functions $v(x_3)$.

The general solution of Eq. (72) is given in the form

$$v(x_3) = \sum_{n=1}^{4} M_{\mathrm{n}} \exp(\mathrm{i}\zeta \Upsilon x_3), \tag{75}$$

where M_{n} are the real and/or complex constants. Substitution of Eq. (75) into Eq. (72) gives the following characteristic equation that Υ satisfies it.

$$(\mu - \tau)\Upsilon^4 + 2(2\mu^* - \mu)\Upsilon^2 + (\mu + \tau) = 0. \tag{76}$$

This equation is the same form of Eq. (60) and its roots are classified into the elliptic complex (EC), elliptic imaginary (EI), hyperbolic (H) or parabolic (P) regimes depending on the current state of stress and internal variables. In each of these regimes, diffuse bifurcations are possible and, in fact, in each regime analysis can be done leading to the appropriate eigenvalue equation. The evaluation of the eigenvalue equation is similar to that for plane strain; Hill and Hutchinson (1975), where the results are summarized with considering subloading surface model with tangential stress rate.

Elliptic complex regime:

The elliptic regime can be subdivided into portions where the roots are complex and imaginary. In the elliptic complex region, the solution (75) for the symmetric modes has the form

$$v(x_3) = \mathrm{Re}[M\sin(\zeta \Upsilon x_3)], \tag{77}$$

where Re[ ] denotes the real part of [ ], M is a complex constant, and $\Upsilon = p \pm \mathrm{i}q$ are any complex roots of Eq. (76) Similarly, the solution (75) for the anti-symmetric modes has the form

$$v(x_3) = \mathrm{Re}[M\cos(\zeta \Upsilon x_3)], \tag{78}$$

Substituting Eqs. (77) and (78) into boundary conditions (74) leads to an eigenvalue equation of the form

$$\frac{q\sin(2\omega p)}{p\sinh(2\omega q)} = \pm\frac{\left(\frac{\mu/\tau-1}{\mu/\tau+1}\right)^{1/2} + 2(\mu^*/\tau-1)}{\left(\frac{\mu/\tau-1}{\mu/\tau+1}\right)^{1/2} - 2(\mu^*/\tau-1)}, \tag{79}$$

where $\omega = \zeta a_3 = m\pi a_3/2a_1$ is the wavelength, beside the $(+)$ sign applies for the symmetric modes, and the $(-)$ sign applies for the anti-symmetric modes. For both the symmetric and anti-symmetric modes, the real and imaginary parts, p and q satisfy the following equations.

$$\left.\begin{aligned} p^2+q^2 &= \left(\frac{\mu/\tau+1}{\mu/\tau-1}\right)^{1/2}, \\ p^2-q^2 &= \frac{2\mu^*/\mu-1}{\tau/\mu-1}. \end{aligned}\right\} \tag{80}$$

Elliptic imaginary regime:

In the elliptic imaginary regime, there are the symmetric modes of the form

$$v(x_3) = M\sinh(\zeta p x_3) + N\sinh(\zeta q x_3), \tag{81}$$

and the anti-symmetric modes are of the form

$$v(x_3) = M\cosh(\zeta p x_3) + N\cosh(\zeta q x_3), \tag{82}$$

where both M and N are the real constants now. p and q are positive and related to the coefficients of Eq. (76). In the elliptic imaginary regime, the roots of Eq. (76) have the form $\pm ip$ and $\pm iq$. The substitution of Eq. (81) into the boundary conditions (74) yields the eigenvalue equation for the symmetric modes:

$$\frac{p\tanh(\omega q)}{q\tanh(\omega p)} = \left(\frac{p^2+1}{q^2+1}\right)^2. \tag{83}$$

Repeating this for the anti-symmetric modes (82) gives

$$\frac{p\tanh(\omega p)}{q\tanh(\omega q)} = \left(\frac{p^2+1}{q^2+1}\right)^2, \tag{84}$$

where p and q for both the symmetric and the anti-symmetric modes satisfy the following equations.

$$\left.\begin{aligned} \frac{1}{2}(p^2+q^2) &= \frac{2\mu^*/\mu-1}{\tau/\mu-1}, \\ \frac{1}{2}(p^2-q^2) &= -\frac{((2\mu^*/\mu-1)^2+(\tau/\mu)^2-1)^{1/2}}{\tau/\mu-1}. \end{aligned}\right\} \tag{85}$$

Parabolic regime:

The general solution (75) for the symmetric modes in the parabolic regime has the form

$$v(x_3) = M\sin(\zeta p x_3) + N\sinh(\zeta q x_3) \tag{86}$$

and for the anti-symmetric modes

$$v(x_3) = M\cos(\zeta p x_3) + N\cosh(\zeta q x_3), \tag{87}$$

where p and iq the positive real and imaginary roots of Eq. (76). The substitution of Eqs. (86) and (87) into the boundary conditions (74) yields the eigenvalue equation for the symmetric modes

$$\frac{q\tan(\omega p)}{p\tanh(\omega p)} = \left(\frac{q^2+1}{p^2-1}\right)^2 \tag{88}$$

and for the anti-symmetric modes

$$\frac{q\tanh(\omega q)}{p\tan(\omega p)} = -\left(\frac{q^2+1}{p^2-1}\right)^2, \tag{89}$$

where p and q for both the symmetric and the anti-symmetric modes satisfy the following equations.

$$\left.\begin{aligned} \frac{1}{2}(p^2+q^2) &= -\frac{((2\mu^*/\mu-1)^2+(\tau/\mu)^2-1)^{1/2}}{\tau/\mu-1}, \\ \frac{1}{2}(p^2-q^2) &= \frac{2\mu^*/\mu-1}{\tau/\mu-1}. \end{aligned}\right\} \tag{90}$$

Hyperbolic regime:

In the hyperbolic regime, the appropriate symmetric modes are

$$v(x_3) = M\sin(\zeta p x_3) + N\sin(\zeta q x_3) \tag{91}$$

and the appropriate anti-symmetric modes are

$$v(x_3) = M\cos(\zeta p x_3) + N\cos(\zeta q x_3), \tag{92}$$

where p and q are positive roots of Eq. (76). The substitution of Eqs. (91) and (92) into the boundary conditions (74) yields the eigenvalue equation for the symmetric modes

$$\frac{q\tan(\omega p)}{p\tan(\omega q)} = -\left(\frac{q^2-1}{p^2-1}\right)^2 \tag{93}$$

and for the anti-symmetric modes

$$\frac{q\tan(\omega q)}{p\tan(\omega p)} = -\left(\frac{q^2-1}{p^2-1}\right)^2, \tag{94}$$

where p and q for both the symmetric and anti-symmetric modes satisfy the following equations:

$$\left.\begin{aligned} \frac{1}{2}(p^2+q^2) &= \frac{2\mu^*/\mu-1}{\tau/\mu-1}, \\ \frac{1}{2}(p^2-q^2) &= -\frac{((2\mu^*/\mu-1)^2+(\tau/\mu)^2-1)^{1/2}}{\tau/\mu-1}. \end{aligned}\right\} \tag{95}$$

Since the localized bifurcation can be seen in soil specimens and the diffuse bifurcation modes occur before localization, it is meaningful to discuss geometrical diffuse modes. Although the diffuse bifurcation modes are investigated in the hyperbolic and parabolic regimes mathematically on the assumption that the localization takes place on the EC–H boundary, we discuss here only the diffuse modes in the elliptic regime.

Fig. 8 represents the bifurcation regimes as a function of the dimensionless variables $\tau/2\mu^*$ and $\mu/2\mu^*$ by the dotted curves. The geometric diffuse bifurcation modes appear in the elliptic, hyperbolic and parabolic regimes. The $(\tau/2\mu^*, \mu/2\mu^*)$ trajectories for several levels of material parameter a ranging from 0.0 to 1.5 in the normal-yield state (a) $R = 1.0$ and the subyield states (b) $R = 0.95$ and (c) $R = 0.90$ for $u_R = 10$ are also depicted in Fig. 8. The trajectories pass through the elliptic complex, the elliptic imaginary, the hyperbolic and the parabolic domains with the variation of parameter a. In the case of $R = 1.0$ and $R = 0.95$, i.e. near the normal-yield state, the trajectories monotonically rise up to the EC–H boundary, while the larger

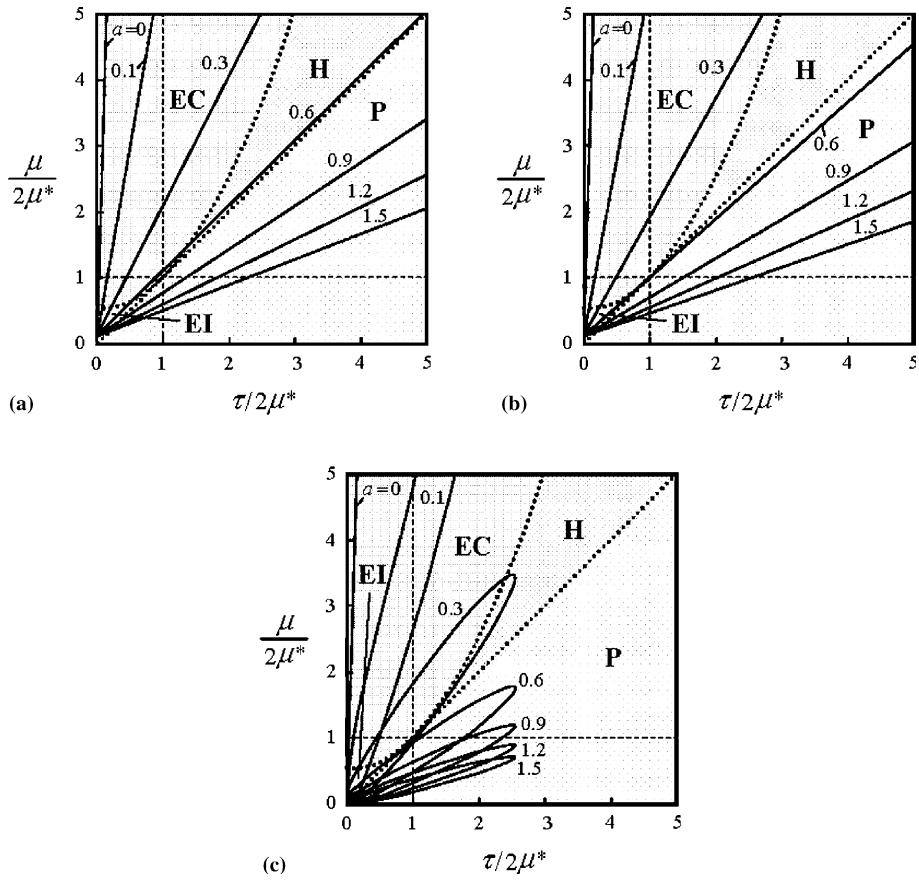

Fig. 8. The $(\tau/2\mu^*, \mu/2\mu^*)$ trajectories with the variation of the material parameter a in the normal-yield state (a) $R = 1.0$ and the subyield states (b) $R = 0.95$ and (c) $R = 0.90$ for $u_R = 10$.

material parameter a makes it easier to pass through the boundary with the increase in χ, since both $\tau/2\mu^*$ and $\mu/2\mu^*$ become infinite as the denominator μ^* becomes zero with the increase in χ, as shown in Fig. 5. In the case of $R = 0.90$, on the other hand, the $(\tau/2\mu^*, \mu/2\mu^*)$ trajectories first rise up with the increase in χ, but suddenly turn back to the origin, since μ^* does not become zero but inversely increases with the increase of lower R, as shown in Fig. 5. Here, it should be noted for the case $a = 0$, i.e. the original subloading surface model without the tangential stress rate effect, the trajectory monotonically rises up and could be achieved only for the instant $\mu^* = 0$.

Fig. 9 shows the lowest bifurcation stress as a function of the wavelength of the diffuse modes $\omega = m\pi a_3/2a_1$ obtained for the symmetric (Fig. 9 (a)) and the anti-symmetric (Fig. 9 (b)) elliptic complex modes of bifurcation in several values $2\mu^*/\mu$. The $(\tau/2\mu^*, \omega)$ trajectories for several levels of the normal-yield ratio $R = 0.89$, 0.90, 1.0 for $u_R = 10$ are depicted in Fig. 9. In the case of $R = 1.0$ i.e. near the normal-yield state, the trajectories rise up with the increase in ω and then turn down, while in the case of subyield states ($R = 0.89$ and $R = 0.90$) the trajectories rise up briefly.

We also consider here the long wavelength limit ($\omega \to 0$) and the short wavelength limit ($\omega \to \infty$) of the eigenvalue equation in EC and EI Regimes.

In the elliptic complex regime, noting that $\lim_{\omega\to 0} q\sin(2\omega p)/p\sinh(2\omega q) = 1$ corresponding to the long wavelength limit, the following equation is obtained from Eq. (79) for symmetric modes

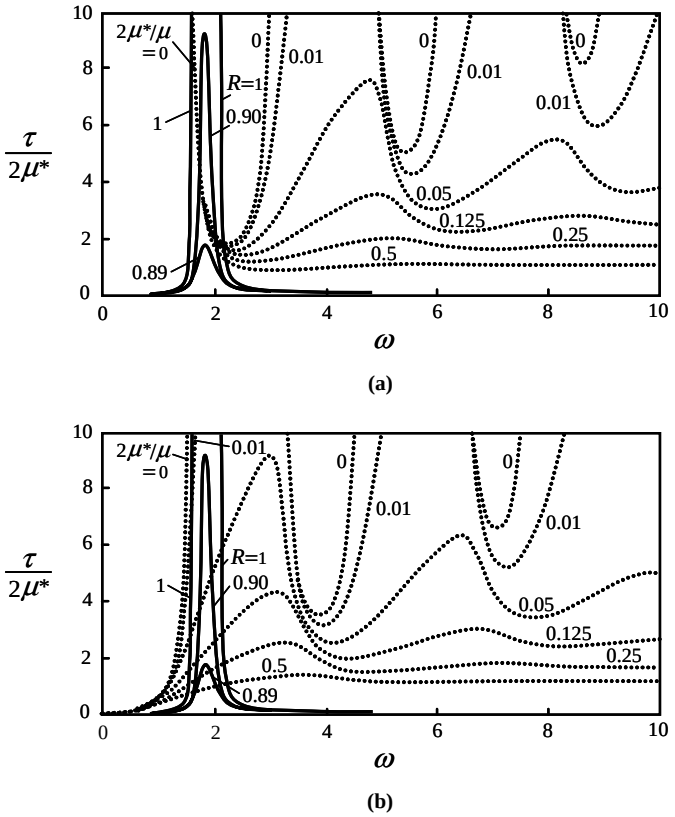

Fig. 9. Lowest bifurcation stress with the variation of $2\mu^*/\mu$ for (a) the symmetric modes and (b) the anti-symmetric modes.

$$\frac{\tau}{2\mu^*} = 1 \tag{96}$$

and for anti-symmetric models leads to $\tau \to 0$. Alternatively, sin( ) can be written as the series representation, then for small values of ω and the first two terms, Eq. (79) can be factored for the symmetric modes as

$$\frac{\tau}{2\mu^*} = 1 + \frac{1}{3}\omega^2\left[\frac{\tau}{2\mu^*} - \left(\frac{\tau}{2\mu^*} - 1\right)\left(\frac{2\mu^* - \mu}{\mu - \tau}\right)\right] \tag{97}$$

and for anti-symmetric modes as

$$\frac{\tau}{2\mu^*} = \frac{1}{3}\omega^2\left[\left(\frac{\tau}{2\mu^*} - 1\right)\left(\frac{\mu + \tau}{\mu - \tau}\right) - \left(\frac{\tau}{2\mu^*}\right)\left(\frac{2\mu^* - \mu}{\mu^* - \tau}\right)\right]. \tag{98}$$

In the short wavelength limit ($\omega \to \infty$), noting that $\lim_{\omega\to\infty} q\sin(2\omega p)/p\sinh(2\omega q) = 0$, the following equation is obtained from Eq. (79) for both the symmetric and anti-symmetric modes in the elliptic complex regime.

$$\frac{\tau}{2\mu^*} = 1 + \frac{\tau}{2\mu^*}\left(\frac{\mu - \tau}{\mu + \tau}\right)^{1/2}. \tag{99}$$

The $(\tau/2\mu^*, \mu/2\mu^*)$ trajectories of the EC regime for the typical width to height ratios a_3/a_1 of soil specimens used in experiments ranging from 0.4 to 0.6 for the symmetric modes and 0.4–1.0 for the

anti-symmetric modes are depicted in Fig. 10(a) and (b), respectively. Taking into account that diffuse bifurcation modes are observed experimentally for a_3/a_1 between 0.4 and 0.6 for the symmetric modes (bulging) and between 0.4 and 1.0 for the anti-symmetric modes (buckling), it can be stated that the wavelength ω is near to the peak of the eigenstress by the numerical results (see Fig. 9). The $(\tau/2\mu^*, \mu/2\mu^*)$ trajectories for the long wavelength limit $(\omega \to 0)$ Eq. (96) and the short wavelength limit $(\omega \to \infty)$ Eq. (99) for the symmetric modes are shown in Fig. 10(a) by the dashed line and curve, respectively.

When the elliptic imaginary regime for the long and short wavelength limit are considered, the eigenvalue equations (83) and (84) can be rewritten regarding to Eq. (85) as

$$\frac{q\tanh(\omega p)}{p\tanh(\omega q)} = \frac{(\tau/2\mu^* - 1)q^2 + \tau/2\mu^*}{(\tau/2\mu^* - 1)p^2 + \tau/2\mu^*}, \tag{100}$$

for the symmetric modes

$$\frac{p\tanh(\omega p)}{q\tanh(\omega q)} = \frac{(\tau/2\mu^* - 1)p^2 + \tau/2\mu^*}{(\tau/2\mu^* - 1)q^2 + \tau/2\mu^*}, \tag{101}$$

for the anti-symmetric modes.

In the long wavelength limit for the EI regime, since $\lim_{\omega\to 0} \tanh(\omega p)/\tanh(\omega q) = p/q$ and $p > q$ by (85), the left sides of Eqs. (100) and (101) must be greater that one. Therefore, considering this condition for the symmetric modes leading to

$$\frac{\tau}{2\mu^*} > 1 + \frac{\tau}{2\mu^*}\left(\frac{\mu - \tau}{\mu + \tau}\right)^{1/2} \tag{102}$$

and for the anti-symmetric modes leading to

$$\frac{\tau}{2\mu^*} < 1 + \frac{\tau}{2\mu^*}\left(\frac{\mu - \tau}{\mu + \tau}\right)^{1/2}. \tag{103}$$

In the short wavelength limit for the EI regime, noting that $\lim_{\omega\to 0} \tanh(\omega p)/\tanh(\omega q) = 1$, Eq. (99) is obtained from Eqs. (100) and (101) for both the symmetric and the anti-symmetric modes again. In fact, the short wavelength limit is the interface between the regions that are defined in the long wavelength limit by Eqs. (102) and (103).

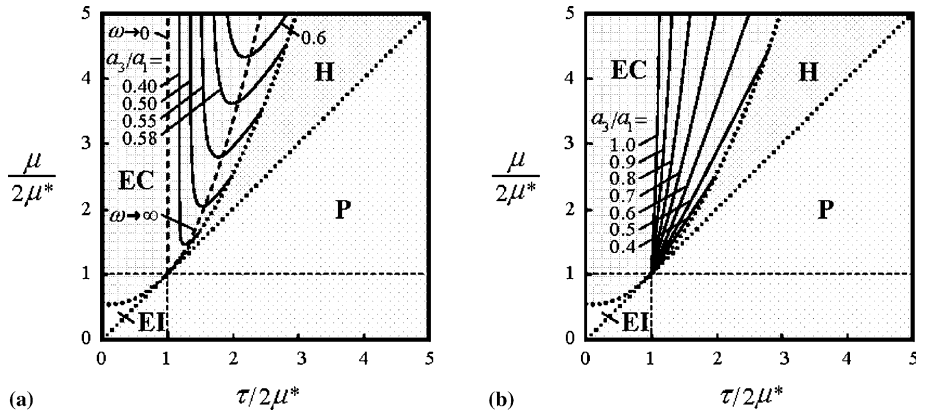

Fig. 10. The $(\tau/2\mu^*, \mu/2\mu^*)$ trajectories with the variation of typical width to height ratios a_3/a_1 for (a) the symmetric modes and (b) the anti-symmetric modes.

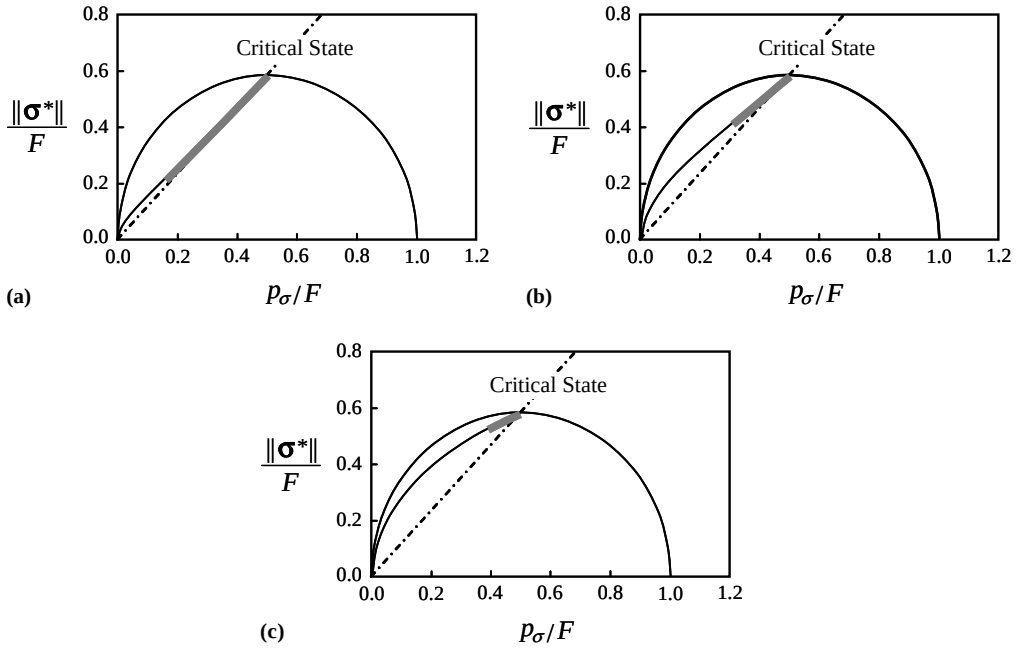

Fig. 11. Possible regions of diffuse bifurcation mode illustrated in the non-dimensional stress plane $(p_\sigma/F, \|\sigma^*\|/F)$ for three levels of the material parameter u_R: (a) $u_R = 1$, (b) $u_R = 10$ and (c) $u_R = 100$.

The regions in the stress space where the diffuse bifurcation modes of deformation can be induced are depicted in Fig. 11 for the three levels of the material parameter: (a) $u_R = 1$, (b) $u_R = 10$ and (c) $u_R = 100$. Since these regions are longer compared to the shear band regions in Fig. 7, it is induced and confirmed that the diffuse modes trigger the pre-peak localization of deformation observed for soils experimentally. Further, it is found that that the lower material parameter u_R gives a wider region of stress for the geometric diffuse formation, inducing the inelastic deformation from the lower value of R. It should be noted that the diffuse bifurcation mode is formed for stress ratios lower than the critical state in the case of $R = 1$, but it is done even for stress ratios higher than the critical state in the case of $R < 1$, while the range of stresses inducing the diffuse bifurcation mode is affected by the material parameter u_R.

8. Concluding remarks

The bifurcations of a rectangular soil specimen subjected to plane strain loading under the undrained conditions including both shear band modes and diffuse modes were analyzed incorporating the subloading surface model with the tangential stress rate effect. The main results obtained are as follows:

(i) The analytical solutions for the inception of the localized bifurcation and the diffuse bifurcation modes are derived, which are classified into the elliptic complex, elliptic imaginary and hyperbolic and parabolic regimes.
(ii) The incorporation of the tangential-plastic strain rate has no influence on the instantaneous shear moduli μ^*, but lowers the instantaneous shear moduli μ.
(iii) The inclination angle of shear bands is predicted to increase by the tangential stress rate effect.

(iv) The tangential-plastic strain rate term makes it easy to fulfill the necessary conditions of the formation of the bifurcation for not only normal-yield, but also subyield states.
(v) The formation of the shear band and the diffuse bifurcation are affected markedly by the material parameter R in the normal-yield ratio prescribing the approaching degree of stress to the normal-yield state.

Acknowledgements

The authors would like to express their sincere gratitude to Professor I. Vardoulakis, Department of Mechanics, Faculty of Applied Sciences, National Technical University of Athens, Greece, during visiting the authors' laboratory from October 2002 to February 2003 and providing valuable discussions on this study. This research has been supported partly by the Postdoctoral Fellowship of the Japan Society of the Promotion of Science (JSPS) for Foreign Researchers.

References

Bardet, J.P., 1991. Analytical solutions for the plane-strain bifurcation of compressible solids. J. Appl. Mech. (ASME) 58, 651–657.
Bousshine, L., Chaaba, A., De Saxce, G., 2001. Softening in stress–strain curve for Drucker–Prager non-associated plasticity. Int. J. Plasticity 17, 21–46.
Chau, K.T., Rudnicki, J.W., 1990. Bifurcations of compressible pressure-sensitive materials in plane strain tension and compression. J. Mech. Phys. Solids 38, 875–898.
Gutierrez, M., Ishihara, K., Towhata, I., 1991. Flow theory for sand during rotation of principal stress direction. Soils Foundations 31, 121–132.
Hashiguchi, K., Ueno, M., 1977. Elastoplastic constitutive laws of granular materials. In: Constitutive Equations of Soils Proc. 9th Int. Conf. Soil Mech. Found. Eng., Spec. Session 9, Tokyo, JSSMFE, pp. 73–82.
Hashiguchi, K., 1980. Constitutive equations of elastoplastic materials with elastic–plastic transition. J. Appl. Mech. (ASME) 47, 266–272.
Hashiguchi, K., 1989. Subloading surface model in unconventional plasticity. Int. J. Solids Struct. 25, 917–945.
Hashiguchi, K., 1993a. Fundamental requirements and formulation of elastoplastic constitutive equations with tangential plasticity. Int. J. Plasticity 9, 525–549.
Hashiguchi, K., 1993b. Mechanical requirements and structures of cyclic plasticity models. Int. J. Plasticity 9, 721–748.
Hashiguchi, K., 1997. The extended flow rule in plasticity. Int. J. Plasticity 13, 37–58.
Hashiguchi, K., 2000. Fundamentals in constitutive equation: continuity and smoothness conditions and loading criterion. Soils Foundations 40, 155–161.
Hashiguchi, K., Tsutsumi, S., 2001. Elastoplastic constitutive equation with tangential stress rate effect. Int. J. Plasticity 17, 117–145.
Hashiguchi, K., Saitoh, K., Okayasu, T., Tsutsumi, S., 2002. Evaluation of typical conventional and unconventional plasticity models for prediction of softening behavior of soils. Geotechnique 52, 561–573.
Hashiguchi, K., Tsutsumi, S., 2003. Shear band formation analysis in soils by the subloading surface model with tangential stress rate effect. Int. J. Plasticity 19, 1651–1677.
Hashiguchi, K., Khojastehpour, M., 2003. Bifurcation analysis of diffuse modes by the subloading surface model with tangential stress rate effect. J. of Appl. Mech. (JSCE) 6, 513–520.
Hashiguchi, K., in press. Generalized plastic flow rule. Int. J. Plasticity.
Hill, R., Hutchinson, J.W., 1975. Bifurcation phenomena in the plane tension test. J. Mech. Phys. Solids 23, 239–264.
Iizuka, A., Yatomi, C., Yashima, A., Sano, I., Ohta, H., 1992. The effect of stress induced anisotropy on shear band formation. Arch. Appl. Mech. 62, 104–114.
Ishihara, K., Towhata, I., 1983. Sand response to cyclic rotation of principal stress directions as induced by wave loads. Soils Foundations 23, 11–26.
Miura, K., Miura, S., Toki, S., 1986. Deformation behavior of anisotropic dense sand under principal stress axes rotation. Soils Foundations 26, 36–52.
Needleman, A., 1979. Non-normality and bifurcation in plane strain tension and compression. J. Mech. Phys. Solids 27, 231–254.
Papamichos, E., Vardoulakis, I., 1995. Shear band formation in sand according to non-coaxial plasticity model. Geotechnique 45, 649–661.

Peric, D., Ayari, M.A., 2002. On the analytical solutions for the three-invariant Cam clay model. Int. J. Plasiticity 18, 1061–1082.
Pradel, D., Ishihara, K., Gutierrez, M., 1990. Yielding and flow of sand under principal stress axes rotation. Soils Foundations 30, 87–99.
Rudnicki, J.W., Rice, J.R., 1975. Conditions for localization of deformation in pressure-sensitive dilatant materials. J. Mech. Phys. Solids 23, 371–394.
Schofield, A.N., Wroth, C.P., 1968. Critical State Soil Mechanics. McGraw-Hill, London.
Vardoulakis, I., 1980. Shear band inclination and shear modulus of sand in biaxial tests. Int. J. Numer. Anal. Meth. Geomech. 4, 103–119.
Vardoulakis, I., 1981. Bifurcation analysis of the plane rectilinear deformation on dry sand samples. Int. J. Solids Struct. 17, 1085–1101.
Yatomi, C., Yashima, A., Iizuka, A., Sano, I., 1989. General theory of shear bands formation by a non-coaxial Cam-clay model. Soils Foundations 29, 41–53.
Young, N.J.B., 1976. Bifurcation phenomena in plane compression test. J. Mech. Phys. Solids 24, 77–91.